
NONINVASIVE INTRACRANIAL PRESSURE ESTIMATION USING SUBSPACE SYSTEM IDENTIFICATION AND BESPOKE MACHINE LEARNING ALGORITHMS: A LEARNING-TO-RANK APPROACH

A PREPRINT

Anni Zhao

Center for Data Science
Emory University
Atlanta, GA 30322, USA
anni.zhao@emory.edu

Ayca Ermis

Center for Data Science
Emory University
Atlanta, GA 30322, USA
ayca.ermis@emory.edu

Jeffrey Robert Vitt

University of California, Davis
Sacramento, CA 95816, USA
jrvitt@ucdavis.edu

Sergio Brasil

São Paulo University
São Paulo, Brazil
sbrasil@alumni.usp.br

Wellington Paiva

São Paulo University
São Paulo, Brazil
wellingtonpaiva@yahoo.com.br

Magdalena Kasprowicz

Wroclaw University of Science and Technology
Wroclaw 50-370, Poland
magdalena.kasprowicz@pwr.edu.pl

Malgorzata Burzynska

Wroclaw Medical University
Wroclaw 50-556, Poland
malgorzata.burzynska@umw.edu.pl

Robert Hamilton

NeuraSignal
Los Angeles, CA 90024, USA
robert@neurasignal.com

Runze Yan

Emory University
Atlanta, GA 30322, USA
runze.yan@emory.edu

Ofer Sadan

Emory University
Atlanta, GA 30322, USA
ofer.sadan@emory.edu

J. Claude Hemphill

University of California, San Francisco
San Francisco, CA 94110, USA
claude.hemphill@ucsf.edu

Lieven Vandenberghe

University of California, Los Angeles
Los Angeles, CA 90095, USA
vandenbe@ucla.edu

Xiao Hu*

Emory University
Atlanta, GA 30322, USA
xiao.hu@emory.edu

January 30, 2026

ABSTRACT

Objective: Accurate noninvasive estimation of intracranial pressure (ICP) remains a major challenge in critical care. We developed a bespoke machine learning algorithm that integrates system identification and ranking-constrained optimization to estimate mean ICP from noninvasive signals. *Methods:* A machine learning framework was proposed to obtain accurate mean ICP values using arbitrary noninvasive signals. The subspace system identification algorithm is employed to identify cerebral hemodynamics models for ICP simulation using arterial blood pressure (ABP), cerebral blood velocity (CBv), and R-wave to R-wave interval (R-R interval) signals in a comprehensive database. A mapping function to describe the relationship between the features of noninvasive signals and the estimation errors is learned using innovative ranking constraints through convex optimization. Patients across multiple clinical settings were randomly split into testing and training datasets for performance evaluation of the mapping function. *Results:* The results indicate that about 31.88% of testing

*Corresponding author: Xiao Hu.

entries achieved estimation errors within 2 mmHg and 34.07% of testing entries between 2 mmHg to 6 mmHg from the nonlinear mapping with constraints. *Conclusion:* Our results demonstrate the feasibility of the proposed noninvasive ICP estimation approach. *Significance:* Further validation and technical refinement are required before clinical deployment, but this work lays the foundation for safe and broadly accessible ICP monitoring in patients with acute brain injury and related conditions.

Keywords Intracranial pressure (ICP) · cerebral hemodynamics · subspace system identification · feature extraction · machine learning · ranking constraints

1 Introduction

Intracranial pressure (ICP) monitoring is invaluable for preventing secondary brain injury in acute brain injury (ABI), including traumatic brain injury (TBI), subarachnoid hemorrhage (SAH), or intracerebral hemorrhage (ICH), and is also indicated in other conditions with suspected intracranial hypertension (IH) (e.g., pseudotumor cerebri). However, the invasive methods for ICP measurement carry the risks of procedural complications and infection, thereby limiting more widespread use Gunn et al. [2020], Carney et al. [2017], Hawryluk et al. [2020]. Consequently, ICP monitoring is confined to a narrow range of acute neurologic conditions in the critical care setting Bratton et al. [2007].

The ongoing development of several accurate and clinically viable noninvasive ICP (nICP) techniques reflect the need for such methods Nicolas et al. [2020]. Despite non-invasive devices aim to monitor different brain physiological phenomena and help detect IH, none of the currently available techniques can provide continuous ICP estimation at the bedside. Such methods include visual evoked potentials del Saz-Saucedo et al. [2016], displacement of the skull Komut et al. [2016], brain tissue resonance Motschmann et al. [2001], cerebrospinal fluid (CSF) flow and cerebral blood flow (CBF) assessed by phase-contrast magnetic resonance imaging (MRI) Czarnik et al. [2007], cerebral blood velocity (CBv) as measured by Transcranial Doppler Ultrasound (TCD) Wei et al. [2025], Rasulo et al. [2022], Panerai et al. [2023], the tympanic membrane displacement Ueno et al. [2003], and electroencephalography (EEG) Pose et al. [2025], acoustic signals through sound propagation from the ear Ganslandt et al. [2017], Herklots et al. [2017], automated pupillometry Oddo et al. [2023] and optic nerve sheath diameter ultrasound Aletreby et al., Martínez-Palacios et al. [2024]. More recently, the Brain4Care (B4C) system was developed by capturing micrometric skull displacements caused by pulsatile changes in ICP Frigieri et al. [2025a,b]. Therefore, this system records skull pulsatile waveforms that have been compared and validated using invasive ICP waveforms Uysal et al. [2025], Brasil et al. [2021], de Moraes et al. [2022].

In recent decades, model-based algorithms have been developed using hemodynamic models and various physiological signals Kashif et al. [2012], Imaduddin et al. [2019]. A fully automated, real-time, and calibration-free algorithm has been proposed for pediatric intracranial pressure (ICP) estimation Fanelli et al. [2019]. In related work, a model-based spectral methodology was developed for noninvasive ICP estimation Jaishankar et al. [2019]. A transfer function based algorithm is adopted to estimate the intracranial pressure noninvasively for idiopathic normal pressure hydrocephalus patients Evensen et al. [2018]. These approaches typically rely on predefined mathematical representations of the cardiovascular and cerebrospinal systems to estimate ICP. While they offer interpretability and are grounded in physiological understanding, their accuracy can be limited by model assumptions and the quality of input signals. To address these limitations, data-driven methods have gained increasing attention. Among them, machine learning has emerged as a promising alternative for nICP estimation, capable of capturing complex, nonlinear relationships that traditional models may overlook Megjhani et al. [2023]. In particular, photoplethysmography (PPG) was introduced to assess its potential for nICP estimation using a range of machine learning algorithms Bradley and Kyriacou [2024]. A systematic review for using machine learning approaches to intracranial pressure prediction can be found in Bradley et al. [2023].

In this study, we present a novel framework that integrates system identification with ranking-constrained machine learning for individualized nICP calibration using multimodal noninvasive signals. By leveraging a multicenter database and comprehensive feature extraction, our approach seeks to advance algorithmic solutions for noninvasive ICP estimation. Unlike conventional methods, it leverages mapping-function learning with problem-specific information and a bespoke machine learning algorithm to overcome past limitations and improve accuracy when selecting optimal dynamic models.

The remainder of this paper is organized as follows. Section 2 describes the proposed algorithm for noninvasive intracranial pressure estimation. Section 3 presents the data processing for the physiological signals. Section 4 presents the experimental results and performance evaluation of the nICP system. Section 5 and 6 provide future research directions and conclusions.

2 Algorithm

This section introduces the proposed algorithm for nICP estimation. Section 2.1 proposes the framework for noninvasive intracranial pressure estimation. Section 2.2 provides a brief introduction of the subspace system identification algorithm. Section 2.3 presents the theoretical formulation and an approximate algorithm to learn mapping-functions. Section 2.6 describes the procedures for noninvasive feature extraction.

2.1 Noninvasive Intracranial Pressure Calibration Framework

From the perspective of dynamic system modeling, the underpinnings of the proposed nICP framework can be understood by analyzing the possible forms of relationships among continuous ICP and noninvasive signals. We adopted the view presented in Fig. 1 for our nICP framework. In this framework, multiple noninvasive signals, $Signal_i, i \in [1, 2, \dots, N]$, are related to ICP via a dynamical system with ICP being one of the output signals. This concept applies to our choice of ABP and CBv for estimating ICP, because it is physiologically plausible that ABP and the R-R interval serve as two inputs to the coupled CBF and CSF circulatory systems, from which both ICP and CBv are outputs. ABP and CBv affect the brain hemodynamics through cerebral perfusion pressure and autoregulation. R-R interval influences the pulsatility of cerebral blood flow and autoregulation interactions. The dynamic system view of ABP, CBv, R-wave to R-wave interval (R-R interval), and ICP is shown on the right-hand side in Fig. 1.

The central idea behind our approach is to first build a collection of dynamic models of the dynamical system and then use an instance of ICP-related signals to locate the optimal model within the collection to simulate ICP for this particular instance. The algorithm framework to realize this idea is shown in Fig. 2. It consists of an offline training and an online implementation section. In offline training, instances of invasive ICP, ABP, CBv, and R-R interval signals are analyzed to yield three databases: 1) linear dynamic models (LDMs), 2) noninvasive features, and 3) mapping-functions. The LDM database contains the input/output models relating ABP, CBV, and R-R interval to ICP built from each signal instance. The feature database contains feature vectors, each of which is extracted from an instance of ABP, CBv, and R-R interval. These feature vectors are used as inputs to the mapping-functions. The mapping-function database contains a mapping-function for each entry in the LDM database to estimate nICP error that would result from using the corresponding LDM on a given instance of ABP, CBv, and R-R interval. The outputs from the mapping-functions would be the nICP estimation errors from the LDMs. To estimate ICP, a new instance of noninvasive signals is first analyzed to extract a feature vector that is further evaluated by each mapping-function in the database. The output from the i -th mapping-function is the estimated nICP error using the i -th model in the database. The estimated nICP errors from all mapping-functions are then ranked so that the LDM with the smallest error will be chosen to simulate nICP. In the following subsections 2.2, 2.3, and 2.6, the algorithms used to build linear dynamic models, learn mapping-functions, and extract noninvasive features are explained in detail.

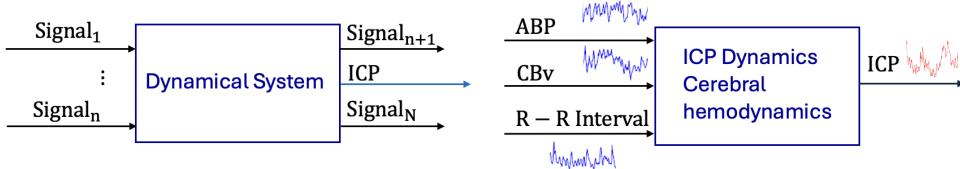


Figure 1: Left: A dynamical system view of ICP and noninvasive signals. Right: A dynamical system view of ICP, ABP, CBv, and R-R interval.

2.2 Linear Dynamic Models

The subspace system identification algorithm is adopted to identify the dynamical system with ABP, CBv, R-R interval as inputs and ICP as output. The structure of the dynamical system is shown in Fig. 1. The subspace system identification algorithm is a data-driven algorithm from the control theory for state-space model identification Katayama [2005]. The identified system can be written in state-space form as,

$$\mathbf{x}_{n+1} = \mathbf{Ax}_n + \mathbf{Bu}_n + \mathbf{w}_n \quad (1)$$

$$y_n = \mathbf{Cx}_n + \mathbf{Du}_n + v_n \quad (2)$$

where $\mathbf{u}_n = [x_{ABP}, x_{CBv}, x_{R-R \text{ interval}}]^T \in \mathbb{R}^{3 \times 1}$ represents the ABP, CBv, and R-R interval signals, $y_n = x_{ICP}$ represents the ICP signal. \mathbf{A} , \mathbf{B} , \mathbf{C} , and \mathbf{D} are the system matrices to be estimated. \mathbf{w}_n is the process noise, v_n is the measurement noise. Given the inputs and outputs of the system, the subspace system identification algorithm estimates

the system matrices by making use of the system inputs \mathbf{u}_n and output y_n . Here, we adopted the optimal model order identified by the MATLAB System Identification Toolbox for each model.

2.3 Mapping Functions Learning

Assume N signal entries are collected as the training data. A single entry is defined as an individual signal segment selected from each recording, with a length of 360 beats. Details can be found in Section 3. From these N signal entries, we identify N LDMs and extract N feature vectors. To learn mapping functions, $N \times N$ model simulations are first performed, where each LDM is used to simulate ICP for each signal entry. By comparing simulated and measured ICP for each entry, we obtain an $N \times N$ error matrix \mathbf{E} . \mathbf{E} is organized such that its i -th row contains errors for i -th entry using N LDMs and the i -th column contains errors from using the i -th LDM to simulate ICP for the N entries. Beginning with using a linear mapping-function for the i -th LDM, we can estimate nICP error for a given noninvasive feature vector $\mathbf{f} \in \mathbb{R}^{d \times 1}$ as $e = \mathbf{f}^T \mathbf{b}_i$ where $\mathbf{b}_i \in \mathbb{R}^{d \times 1}$ is the coefficient vector for this mapping-function. To estimate $\mathbf{b}_i, i = 1, \dots, N$ using error matrix \mathbf{E} and feature matrix \mathbf{F} from the training data, we can formulate the problem:

$$\min_{\mathbf{b}_i} \|\mathbf{F}\mathbf{b}_i - \mathbf{e}_{:,i}\|_2, i = 1, \dots, N \quad (3)$$

where $\mathbf{F} \in \mathbb{R}^{N \times d}$, the i -th row of feature matrix \mathbf{F} is the feature vector from i -th entry. $\mathbf{e}_{:,i} \in \mathbb{R}^{N \times 1}$ is the column vector of error matrix $\mathbf{E} \in \mathbb{R}^{N \times N}$. $\|\cdot\|_2$ is the L_2 norm of a matrix. In essence, we solve N independent least squares problems. The original formulation in Eq. (3) is hereafter referred to as ‘Linear Mapping without Constraints’ for illustration in the following sections.

However, this simple formulation misses an important characteristic that \mathbf{b}_i should have. The order of $e_{i,j}, i, j = 1, \dots, N$ is important because it tells the ranking of LDM models with regard to the accuracy of their nICP estimates for j -th database entry. Therefore, it would be beneficial to learn \mathbf{b}_i s in such a way that $\mathbf{f}_i^T \mathbf{b}_k$ and $\mathbf{f}_i^T \mathbf{b}_l$ obeys the ranking between $e_{i,k}$ and $e_{i,l}$. Obviously, independent learning of each \mathbf{b}_i cannot ensure this important ranking relationship. To incorporate the ranking constraints, we formulate the problem as:

$$\min_{\mathbf{b}_i} \|\mathbf{F}\mathbf{b}_i - \mathbf{e}_{:,i}\|_2 + \gamma \|\boldsymbol{\sigma}\|_2, i = 1, \dots, N \quad (4)$$

$$\text{subject to } \sigma_j \geq 0 \quad (5)$$

$$\boldsymbol{\alpha}_j^T \mathbf{F} \mathbf{B} \boldsymbol{\beta}_j \leq \sigma_j, j = 1, 2, \dots, N \times \binom{N}{2} \quad (6)$$

where $\mathbf{B} \in \mathbb{R}^{d \times N}$ is a matrix with \mathbf{b}_i being the i -th column, $\boldsymbol{\alpha}_j$ is a $N \times 1$ vector with only one nonzero element equal to 1, $\boldsymbol{\beta}_j$ is a $N \times 1$ vector with only two nonzero elements equal to 1 and -1, respectively. For example, $\boldsymbol{\alpha}_j$ could be in the form as $[0 \dots 1 \dots 0]^T$, $\boldsymbol{\beta}_j$ could be in the form as $[0 \dots 1 \dots -1 \dots 0]^T$. So $\boldsymbol{\alpha}_j^T \mathbf{F} \mathbf{B} \boldsymbol{\beta}_j = \mathbf{f}_m^T (\mathbf{b}_k - \mathbf{b}_l)$ expresses one ranking condition for an arbitrary m, k, l depending on the locations of those nonzero elements in $\boldsymbol{\alpha}_j$ and $\boldsymbol{\beta}_j$. Here m is the index for the entry. σ_j is a slack variable for relaxing the constraints so that $\mathbf{f}_m^T (\mathbf{b}_k - \mathbf{b}_l) < 0$ does not need to be strictly satisfied. In the above problem formulation, γ is a hyperparameter that controls the tradeoff between the error of estimating nICP error and the degree of constraint violations. Importantly, the problem is convex, and a global optimal solution exists. However, this is a large-scale problem given the huge number, $N \times \binom{N}{2}$, of constraints because the number of database entries N needs to be big for achieving diversity in the dynamics of stored signals and ensure wide applicability of the resultant nICP system. We also developed an approximate algorithm for linear mapping to speed up the computation and a nonlinear mapping algorithm with kernelization to improve the estimation accuracy. The illustration of various algorithms can be found in Fig. 3.

2.4 An Approximate Algorithm to Learn Mapping Functions

Instead of enforcing all constraints at the same time, we will sequentially solve N sub-problems, the n -th of which will have the following form

$$\min_{\mathbf{b}_n} \|\mathbf{F}\mathbf{b}_n - \mathbf{e}_{:,n}\|_2 + \gamma \|\boldsymbol{\sigma}\|_2 + \rho \|\mathbf{b}_n\|_2 \quad (7)$$

$$\text{subject to } \sigma_l \geq 0, l = 1, \dots, 2N \quad (8)$$

$$\mathbf{f}_j^T \mathbf{b}_n < \min(\hat{e}_{j,L^{-1}(j,n)}) + \sigma_j \quad (9)$$

$$\mathbf{f}_j^T \mathbf{b}_n > \max(\hat{e}_{j,L+(j,n)}) + \sigma_{j+N}, j = 1, \dots, N \quad (10)$$

In this formulation, we assume we have estimated $\mathbf{b}_i, i = 1, \dots, n-1$ before solving \mathbf{b}_n . The incorporation of ranking constraints is done by using two lists:

- $L^+(j, n) = \{k | e_{j,n} > e_{j,k} \& k = 1, \dots, n-1\}$, which collects indices of those $e_{j,k}$ that are smaller than $e_{j,n}$.
- $L^-(j, n) = \{k | e_{j,n} < e_{j,k} \& k = 1, \dots, n-1\}$, which collects indices of those $e_{j,k}$ that are greater than $e_{j,n}$.

Further let $\hat{e}_{j,i} = \mathbf{f}_j^T \hat{\mathbf{b}}_i$ be the estimate of $e_{j,i}$ where $\hat{\mathbf{b}}_i$ is the estimated \mathbf{b}_i . Then, we can see that $\mathbf{f}_j^T \mathbf{b}_n$ needs to be greater than all $\hat{e}_{j,k}$ with k in list $L^+(j, n)$. This condition can be simplified as $\mathbf{f}_j^T \mathbf{b}_n > \max(\hat{e}_{j,L^+(j,n)})$. Similarity, $\mathbf{f}_j^T \mathbf{b}_n$ needs to be smaller than all $\hat{e}_{j,k}$ with k in list $L^-(j, n)$ that leads to $\mathbf{f}_j^T \mathbf{b}_n < \min(\hat{e}_{j,L^-(j,n)})$. Given the above derivation, the maximal number of constraints is $2N$ at each step. When conflicts occur where $\min(\hat{e}_{j,L^-(j,n)}) < \max(\hat{e}_{j,L^+(j,n)})$, we randomly keep only one of the two constraints. Also, slack variable σ is introduced as well to relax the constraints as a usual practice. Here, a regularization term $\rho \|\mathbf{b}_i\|_2$ is introduced to deal with the under-determined system when the feature dimension is higher than the number of samples. The approximation algorithm with ranking constraints formulated above is hereafter referred to as ‘Linear Mapping with Constraints’ for illustration in the paper.

2.5 Kernelization to Achieve Nonlinear Mapping Functions

To further enhance the flexibility of the mapping-function, we demonstrate (after dropping all subscripts and introducing a L2 regularization term) that the above linear solution can be expressed solely in the form of inner products among various feature vectors and hence a “kernel trick” can be played to replace those inner products with a nonlinear kernel function. In this way, we obtain a nonlinear mapping that takes into consideration the ranking constraints. This process can be compactly expressed as:

Step 1): re-formulation in standard form

$$\min_{\mathbf{b}_i} \|\mathbf{F}\mathbf{b}_i - \mathbf{e}_{:,i}\|_2 + \gamma \|\sigma\|_2 + \rho \|\mathbf{b}_i\|_2 \quad (11)$$

$$\text{subject to } \sigma_j \geq 0 \& \mathbf{f}_j^T \mathbf{b}_i \leq \omega_j + \sigma_j, j = 1, \dots, N \quad (12)$$

Step 2): Assume that $\mathbf{b}_i = \mathbf{F}^T \mathbf{u}$, then solution must be in row space of \mathbf{F}

$$\min_{\mathbf{u}} \|\mathbf{F}\mathbf{F}^T \mathbf{u} - \mathbf{e}_{:,i}\|_2 + \gamma \|\sigma\|_2 + \rho \mathbf{u}^T \mathbf{F} \mathbf{F}^T \mathbf{u} \quad (13)$$

$$\text{subject to } \sigma_j \geq 0 \& \mathbf{f}_j^T \mathbf{F}^T \mathbf{u} \leq \omega_j + \sigma_j, j = 1, \dots, N \quad (14)$$

Step 3): substitution of $\mathbf{z} = \mathbf{F}\mathbf{F}^T \mathbf{u}$

$$\min_{\mathbf{z}} \|\mathbf{z} - \mathbf{e}_{:,i}\|_2 + \gamma \|\sigma\|_2 + \rho \mathbf{z}^T (\mathbf{F}\mathbf{F}^T)^{-1} \mathbf{z} \quad (15)$$

$$\text{subject to } \sigma_j \geq 0 \& z_j \leq \omega_j + \sigma_j, j = 1, \dots, N \quad (16)$$

where $\mathbf{u} \in \mathbb{R}^{N \times 1}$, $\mathbf{z} \in \mathbb{R}^{N \times 1}$. w_j is the ranking constraints from section 2.4. ρ and γ are the hyperparameters that controls the trade-off between different terms in the objective function. After estimating \mathbf{z} as the solution to the problem formulated at Step 3), an estimate of nICP error for a new feature vector \mathbf{f}_{N+1} can be obtained as $e_{N+1} = \mathbf{f}_{N+1}^T \mathbf{F}^T (\mathbf{F}\mathbf{F}^T)^{-1} \mathbf{z}$ where only inner products among rows of \mathbf{F} and between rows of \mathbf{F} and \mathbf{f}_{N+1} are involved. By replacing inner products with kernel functions $k(x, y)$, we have $e(\mathbf{f}_{N+1}) = \sum_{i=1}^N k(\mathbf{f}_{N+1}^T, \mathbf{f}_{i,:}) \mathbf{K}_{i,:}^{-1} \mathbf{z}$ where \mathbf{K}^{-1} is the inverse of kernel matrix \mathbf{K} of training features with $\mathbf{K}_{i,j} = k(\mathbf{f}_{i,:}, \mathbf{f}_{j,:})$. Here Gaussian function and polynominal function are adopted as the kernel function $k(\mathbf{x}, \mathbf{y})$ and the regularization term $\rho \|\mathbf{b}_i\|_2$ is introduced for the nonlinear mapping function to deal with the under-determined system when the feature dimension is higher than the number of samples.

The Gaussian kernel function is defined as,

$$k(\mathbf{x}, \mathbf{y}) = e^{-\frac{|\mathbf{x}-\mathbf{y}|^2}{2t^2}} \quad (17)$$

where $|\mathbf{x} - \mathbf{y}|^2$ stands for the Euclidean distance squared between the two feature vectors, t stands for the smoothing parameter of the kernel function. Here we adopted the median value of the distance matrix as the smoothing parameter.

The polynominal function is defined as,

$$k(\mathbf{x}, \mathbf{y}) = (\mathbf{x}' * \mathbf{y})^d \quad (18)$$

where d is the polynomial degree. Here we adopted $d = 2$. For both linear mapping and nonlinear mapping, the hyperparameters are generated in a certain range and the optimal hyperparameters are selected based on a metric defined using the estimated nICP error from the training datasets with cross validation. The kernelized nonlinear mapping function formulation is hereafter referred to as ‘Nonlinear Mapping with Gaussian Kernel’ and ‘Nonlinear Mapping with Polynomial Kernel’ for illustration in the paper.

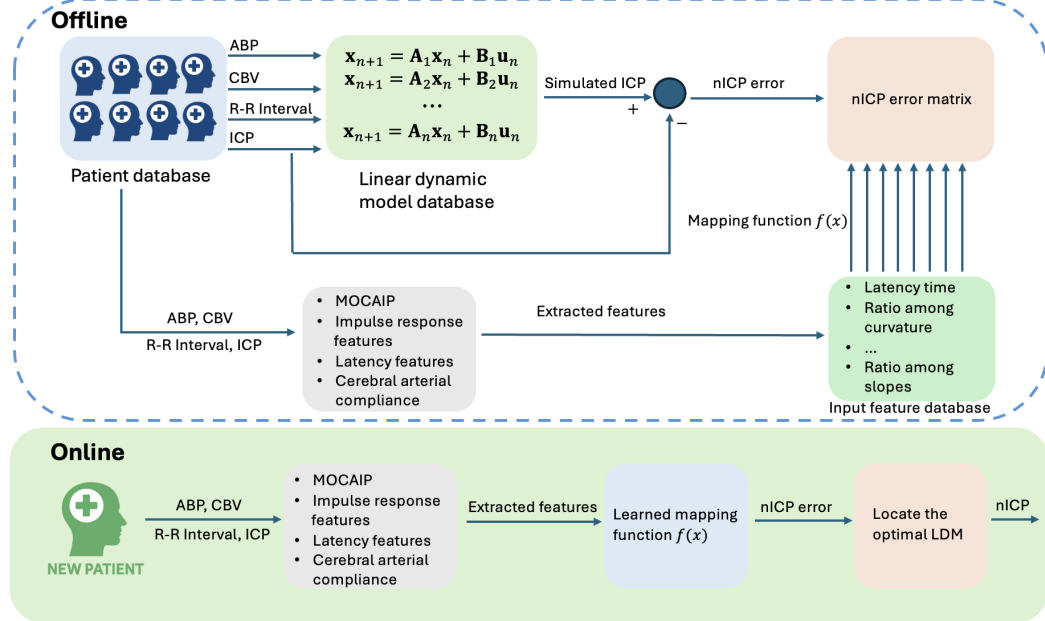


Figure 2: Block diagram of the nICP calibration framework. The contents within the blue dashed line represent the offline training procedure. The green area represents the online training procedure.

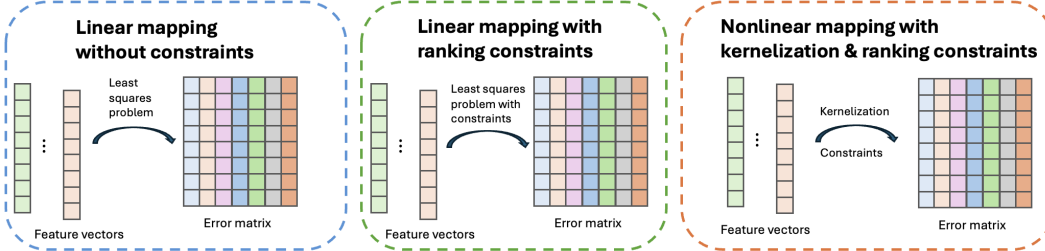


Figure 3: Summary of various algorithms to learn the mapping function. Left: Linear mapping function learning without constraints. Middle: Linear mapping function learning with constraints. Right: Nonlinear mapping with kernelization & ranking constraints.

2.6 Noninvasive Features

In this section, the algorithm to compute noninvasive features is introduced in detail. Four types of feature vectors were computed and concatenated into one vector as input to the mapping-functions. The first type of feature vector is the impulse response features. The slow wave of ABP and R-R interval are selected as the inputs, the slow wave of CBV is treated as the output. Slow waves in ABP, and CBV can be described by oscillatory modes between 0.013 and 0.155 Hz Martinez-Tejada et al. [2021]. The impulse response constructed from the model identified using slow-wave signals is treated as an impulse-response feature vector. The input signals are the slow waves from ABP and the R-R interval. The output signal is the slow wave from CBV. The second type of feature vector contains the latency features. The latency features are extracted from ABP and CBFV signals by computing the latency time between the onsets and the R peak in the ECG signal. The third type of feature vector is the cerebral arterial compliance features. The cerebral arterial compliance features are extracted by fitting the first derivative of ABP versus CBV on a pulse-by-pulse fashion.

The fourth type of feature vector is the morphological clustering and analysis of continuous intracranial pressure (MOCAIP) feature vector Hu et al. [2010], Hu et al. [2008]. The image on the right-hand side of Fig. 4 shows the landmarks on a CBv pulse and the table shows the MOCAIP feature vector was extracted as the 128 CBv pulse morphological metrics. It has been demonstrated that MOCAIP can be applied to the CBv signal. These metrics of the CBv pulses were reliably extracted using our MOCAIP algorithm Kim et al. [2011a], Kim et al. [2011b]. The MOCAIP algorithm automates the analysis of CBv pulses by designating the locations of three sub-peaks and valleys in the waveform as shown in Fig. 4. We demonstrated that these metrics can be used as features to detect elevated ICP Xie et al. [2013]. In this paper, the concatenated feature vector is adopted as input to the mapping-function to evaluate the performance of LDM for nICP estimation.

2.7 Pre- and Post-Processing

To further investigate the performance of the learned mapping function, pre- and post-processing were applied to the identification systems, input signals, and estimated mean nICP. Table 1 summarizes the different scenarios in nICP estimation. ‘Normalization’ refers to applying the Min-Max normalization method to the input signals prior to nICP evaluation. ‘Median value’ and ‘Mean value’ stand for selecting the median and mean values of the mean nICP from the five identified systems with the smallest estimated nICP error by their mapping functions, respectively. ‘✓’ indicates the inclusion of that computation. ‘✗’ indicates the exclusion of that computation.

Table 1: Summary of various scenarios in nICP estimation.

Scenario	Normalization	Median value	Mean value
N0	✗	✗	✗
N0-Med	✗	✓	✗
N0-Mean	✗	✗	✓
N1	✓	✗	✗
N1-Med	✓	✓	✗
N1-Mean	✓	✗	✓

3 Data Preprocessing

This section introduces the data collection and preprocessing for noninvasive intracranial pressure estimation. We adopted datasets from various locations to develop a comprehensive database of multimodality monitoring signals for brain-injured patients. The database includes electrocardiogram (ECG), ABP, CBv, and ICP signals, collected from the University of California, Los Angeles (UCLA), University of California, Davis (UCD), Emory University (IRB: STUDY00004039), University of São Paulo (USP) Medical School Hospital (IRB: NCT03144219), NeuraSignal, Inc (IRB: 14430), and Wrocław Medical University (WMU) in Poland (IRB: KB-620/2020, KB-133/2023). The data collection protocols were approved by the Institutional Review Boards of Emory University, and the data from these institutions were obtained under Emory-approved Data Use Agreements (DUAs).

Table 2: Summary of the datasets from various locations.

Datasets	Number of Patients	ICP Monitoring Type	Range of ICP (mmHg)	Standard Deviation (mmHg)	Mean ICP (mmHg)	Median ICP (mmHg)
UCLA	75	N/A	[-29.06, 62.61]	8.24	14.28	13.39
UCD	25	EVD, parenchymal monitor	[-7.57, 58.85]	5.65	13.35	13.32
USP	35	Intraventricular catheter	[-1.52, 37.33]	6.15	13.74	12.59
WMU	19	Intraparenchymal probe	[-7.72, 36.94]	7.15	10.32	9.02
NeuraSignal	1	Intraventricular catheter	[5.92, 26.07]	3.63	14.73	14.66
Emory	1	EVD	[5.52, 45.23]	2.69	10.25	9.29
Total	156	N/A	[-29.06, 62.61]	6.75	13.36	12.97

EVD: External ventricular drain.

There are 156 patients in total, with 75 from UCLA Kim et al. [2012], 25 from UCD, 35 from USP Medical School Hospital, 19 from WMU, 1 from NeuraSignal, and 1 from Emory University. The data selection process is a critical step in preparing datasets for analysis or model development. To ensure compatibility with the algorithm developed, in this study, the data selection process involves evaluating the completeness of the data, ensuring the quality of the data, and selecting valid features. Consequently, the number of patients across locations differs according to subject enrollment and data quality. A summary of the datasets information can be found in Table 2. The main ICP is distributed in the range $[-29.06, 62.61]$ mmHg from brain-injured patients. The majority of the ICP values are concentrated within the range of $[12, 14]$ mmHg with the mean ICP as 13.36 mmHg. The datasets were divided into segments of 360

Table 3: Patient demographics and pathology distribution.

Category	Level	Number	Percentage (%)
Age (years)	Mean	44.50	—
	Median	42	—
Age group	18-39	171	40.33
	40-59	118	27.83
	60-79	123	29.01
	≥ 80	5	1.18
Sex	Female	164	38.68
	Male	259	61.08
Pathology / Diagnosis	Traumatic brain injury (TBI)	118	27.83
	Subarachnoid hemorrhage (SAH)	101	23.82
	Other	205	48.35

heartbeats per entry, resulting in a total of 448 entries. Note that the ICP was collected using various monitoring types and at different measurement locations; this may introduce hydrostatic offsets that affect the estimation results. The demographics and pathology distribution of the entries are shown in Table 3. Note that demographic information is not available for all entries; therefore, we summarize demographics based on 424 entries.

The 360 heartbeats length is chosen as a tradeoff between providing a sufficient number of signal samples for system identification and using a short enough signal segment to avoid violation of the linearity assumption that is used for using a linear dynamic model to model coupled CBF and CSF circulatory systems. To test the performance of the machine learning algorithm, we separated the datasets into training and testing datasets based on patient ID. There are 357 entries randomly selected as training datasets, the rest 91 entries are adopted as testing datasets. For the training datasets, the ICP is distributed in the range of $[-17.81, 60.06]$ mmHg. For the testing datasets, the ICP is distributed in the range of $[-29.06, 69.80]$ mmHg. Among the 448 entries, there are 310 entries with ECG signal and 138 entries without ECG signal. For the datasets with ECG, the ECG signal is adopted to identify peaks for segmentation of other physiological signals. For datasets without ECG, segmentation is performed using the IMS algorithm Karlen et al. [2012] on ABP signal, as the ABP signal offers the highest quality. Then the segmentation of ICP and TCD is performed based on their latency time relative to the ABP signal. The onsets of ICP and TCD are searched in the nearest time window based on the onsets of ABP signal. The relative time search window for TCD and ICP signals is set to $0.5s$ before the onset of the ABP signal and $0.15s$ after it. Here the relative time is determined through trial and errors to guarantee the quality of signal segmentation.

Fig. 4 shows the data processing in general, including the data selection, signal segmentation, and feature extraction. The 448 entries were selected using the following procedures: (1) data completeness and quality check and (2) feature validity check. After the data completeness and quality check, signals from each recording were segmented into entries of 360 beats using the MOCAIP toolbox. Each recording is at least 360 beats long. Each entry was then manually reviewed by verifying the validity of the extracted MOCAIP features. There are 128 features in total, and some representative features are shown on the right-hand side of Figure 4. A flowchart is created as shown in the middle of Fig. 4 to show the segmentation for datasets with ECG and without ECG to obtain the individual entry. All datasets, either non-invasive or invasive, are collected synchronously and resampled at 400 Hz. For entries with ECG, the R-R interval is computed using a general biomedical signal processing toolbox for QRS detection. For entries without ECG, the R-R interval is determined by detecting the onsets of the ABP signal, which serves as a surrogate QRS R peak position. Table 4 gives a summary of the training and testing datasets in terms of the number of entries, number of patients, ECG signal availability. Note that there are 4 testing entries and 3 training entries with a mean ICP below 0 mmHg, which could be due to the measuring position and artifacts.

Table 4: Summary of various scenarios in nICP estimation.

Datasets	Number of entries	Number of patients	Entries w/ ECG ^a	Entries w/o ECG ^b
Training	357	114	274	83
Testing	91	42	36	55

^a Entries w/ ECG: Number of entries with ECG signals. ^b Entries w/o ECG: Number of entries without ECG signals.

4 Results

This section shows the results of noninvasive intracranial pressure estimation. Section 4.1 presents the results of the trained model, evaluated using both the training and testing datasets.

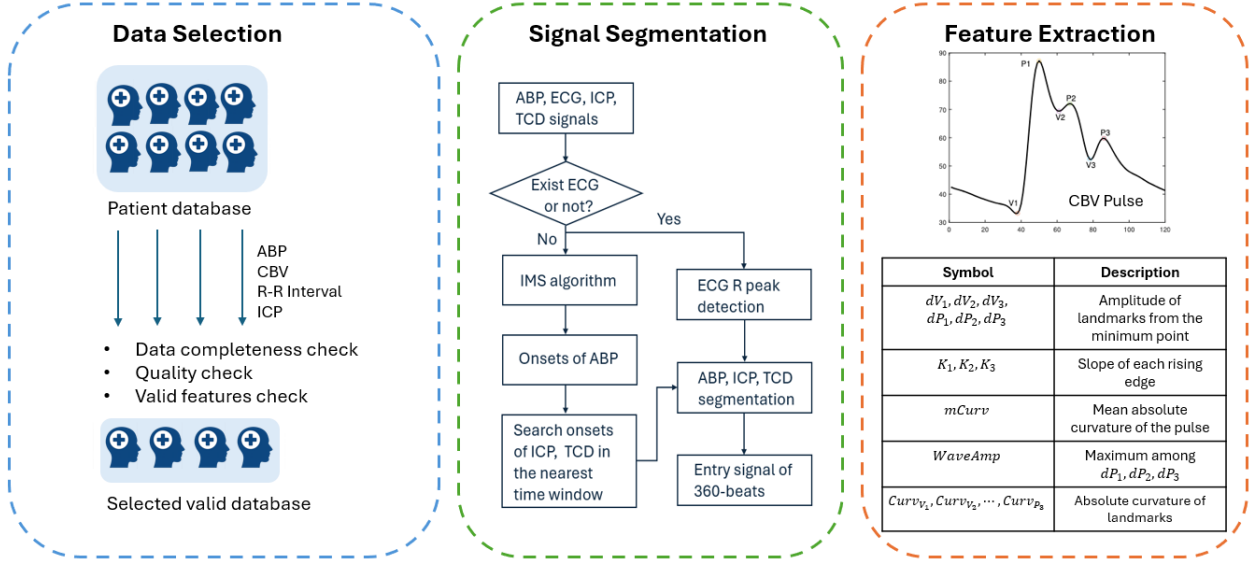


Figure 4: Data processing and feature extraction procedures for nICP estimation. Left: Data selection procedure from the database. Middle: Signal segmentation for signals with and without ECG. Right: Feature extraction for CBV pulse.

4.1 Results from Trained Mapping Functions

The Bland-Altman plot is adopted to show the performance of nICP estimation. Bland-Altman analysis is a common tool adopted in clinical studies to show the agreement between two quantitative methods of measurement Giavarina [2015]. The Bland-Altman plot shows the mean value of the y axis and limits of agreement. Limits of agreement (LOA) is defined as $\text{mean} \pm 1.96 \times \text{standard deviation of the mean value}$. Multiple scenarios in Table 1 are selected to illustrate the estimation accuracy and shown in Table 5. Table 5 summarizes the results from computation scenario N1-Mean for testing entries with linear and nonlinear mappings. It has been observed that the results from N0 and N1 are identical. Similarly, the results from N0-Median and N1-Median are identical, as are the results from N0-Mean and N1-Mean. The averaged value from N1, N1-Median, and N1-Mean is also adopted to show the estimation results in Table 5. The results indicate that normalization exert only a minor influence on the nICP estimation errors. The percentage of estimation errors within 2 mmHg and between 2 mmHg and 6 mmHg are also calculated to demonstrate the accuracy of the estimation results.

Table 5 also shows the nICP estimation results from testing entries with linear mapping function without ranking constraints. In average, there are 20.16% of entries with mean estimation error below 2 mmHg, 23.08% of the estimation errors between 2 mmHg to 6 mmHg. In total, there is 43.24% below 6 mmHg. For the linear mapping function with ranking constraints, there is an average increase of 1.83% in the number of entries with nICP estimation errors below 2 mmHg, and a 22.35% increase in entries with errors between 2 mmHg and 6 mmHg. Overall, N1-Median demonstrates the highest accuracy with 69.25% below 6 mmHg. Compared to the linear mapping function without constraints, incorporating ranking constraints significantly reduces the nICP estimation error, resulting in a 24.18% increase in the number of entries with errors below 6 mmHg.

Based on the results from testing entries with nonlinear mapping function using various kernels, including the Gaussian kernel and the polynomial kernel. The nonlinear mapping with a Gaussian kernel shows the highest accuracy improvement. Compared to linear mapping without constraints, there is 24.57% increment entries in terms of nICP estimation error below 6 mmHg.

Table 5 also summarizes the mean nICP estimation errors for testing entries using linear mapping with and without constraints, as well as nonlinear mapping, at the patient level. At the patient level, the estimation error is calculated based on the patient ID, using the mean estimation error across various entries from the same patient. At the patient level, linear mapping without constraints achieved clinically acceptable accuracy (error below 2 mmHg) Evensen and Eide [2020] in average only 28.58% of the patients. 30.95% of the patients showed moderate accuracy (between 2 mmHg to 6 mmHg). Note that some patients appear in both ranges, resulting in approximately 43.24% of the patients having estimation errors below 6 mmHg.

Table 5: Summary of nICP estimation mean errors below 2 mmHg, and between 2 mmHg and 6 mmHg from testing entries for linear mappings and nonlinear mappings with N1-Median and averaged value from various scenarios.

Algorithms	Evaluation level	Scenarios	$E < 2$ mmHg (%)	$2 \text{ mmHg} < E < 6$ mmHg (%)	$E < 6$ mmHg (%)
Linear Mapping without Constraints	Entry level	N1-Median	25.28	19.79	45.07
		Average	20.16	23.08	43.24
	Patient level	N1-Median	33.33	26.19	50.00
		Average	28.58	30.95	50.00
Linear Mapping with Constraints	Entry level	N1-Median	21.99	47.26	69.25
		Average	21.99	45.43	67.42
	Patient level	N1-Median	30.95	52.38	71.43
		Average	23.81	54.76	69.05
Nonlinear Mapping with Gaussian Kernel	Entry level	N1-Median	31.88	34.07	65.95
		Average	32.24	35.53	67.81
	Patient level	N1-Median	35.71	45.24	69.05
		Average	35.71	47.62	71.43
Nonlinear Mapping with Polynominal Kernel	Entry level	N1-Median	30.78	35.17	65.95
		Average	31.51	36.27	67.78
	Patient level	N1-Median	38.10	45.24	69.05
		Average	38.10	45.24	71.43

Table 6: Summary of nICP estimation errors using mean, standard deviation and median metrics from testing entries for linear mappings and nonlinear mappings.

Algorithms	Evaluation level	Mean	STD	Median
Linear Mapping without Constraints	Entry level	7.99	45.1	5.63
Linear Mapping with Constraints	Entry level	-0.93	7.14	-1.52
Nonlinear Mapping with Gaussian Kernel	Entry level	0.073	6.98	0.15

STD: Standard deviation.

By incorporating the constraints, there is 4.77% decreasing of the patients have estimation errors less than 2 mmHg, 23.81% improvements in the range of 2 mmHg to 6 mmHg, and 21.43% improvements below 6 mmHg. Same for the results computed from the nonlinear mapping with Gaussian and polynomial kernels, there are more than 20% improvements for estimation results below 6 mmHg.

Table 6 shows the summary of nICP estimation errors using mean, standard deviation, and median metrics from testing entries for linear mappings and nonlinear mappings. It is observed that the nonlinear mapping with a Gaussian kernel yields the minimum values in terms of mean estimation error, standard deviation, and median error.

Fig. 5 presents the nICP estimation results using Bland–Altman plots from testing entries for the original linear mapping without constraints, linear mapping with constraints, and nonlinear mapping, including all testing entries as well as those with normal ICP. Normal ICP is defined as a ground truth ICP value below 20 mmHg. Specifically, the N1-Median algorithm is selected to demonstrate the accuracy of the results. Each dot in the figure stands for the mean estimation error from each entry. For linear mapping without constraints, the mean estimation error is around -8 mmHg for testing entries, for normal ICP below 20 mmHg the mean estimation error is about -3 mmHg. Moreover, numerous estimation outliers are observed in the unconstrained linear mapping. We observed that the mean estimation error is around 1 mmHg for testing entries from linear mapping with constraints, indicating good estimation performance once the ranking constraints are included in the linear mapping. For entries with normal ICP the mean estimation error is around 2 mmHg. The trained mapping function performs well for entries with normal ICP.

Fig. 5 also shows the testing entries with N1-Median from nonlinear mapping. From the results, we observed that for all testing entries, it has the minimum mean estimation error as around -0.1 mmHg. The results demonstrate that, overall, the nonlinear mapping yields a smaller mean estimation error across all subjects, accompanied by higher confidence. Fig. 6 shows the distribution comparison between the estimated ICP and the ground truth ICP from nonlinear mapping with Gaussian kernel.

Fig. 7 shows the nICP estimation error as a function of the mean ICP difference between the testing entries and the training entries. The objective is to investigate the influence of the ICP value differences on the training and testing datasets. It is observed that the mean ICP difference between the training and testing entries has a significant influence on the nICP error, with the minimum estimation error occurring around $\Delta_{meanICP} = 1.58$ mmHg. Fig. 8 presents the estimated ICP values from various patients over a prolonged time period using different algorithms. Patients with normal and low ICP are used as examples to illustrate the estimation results. The results indicate that linear mapping without constraints yields the largest estimation error for patients with normal ICP over a long time period as indicated by the patient case with ground truth ICP as 13.46 mmHg, while nonlinear mapping produces the smallest estimation error.

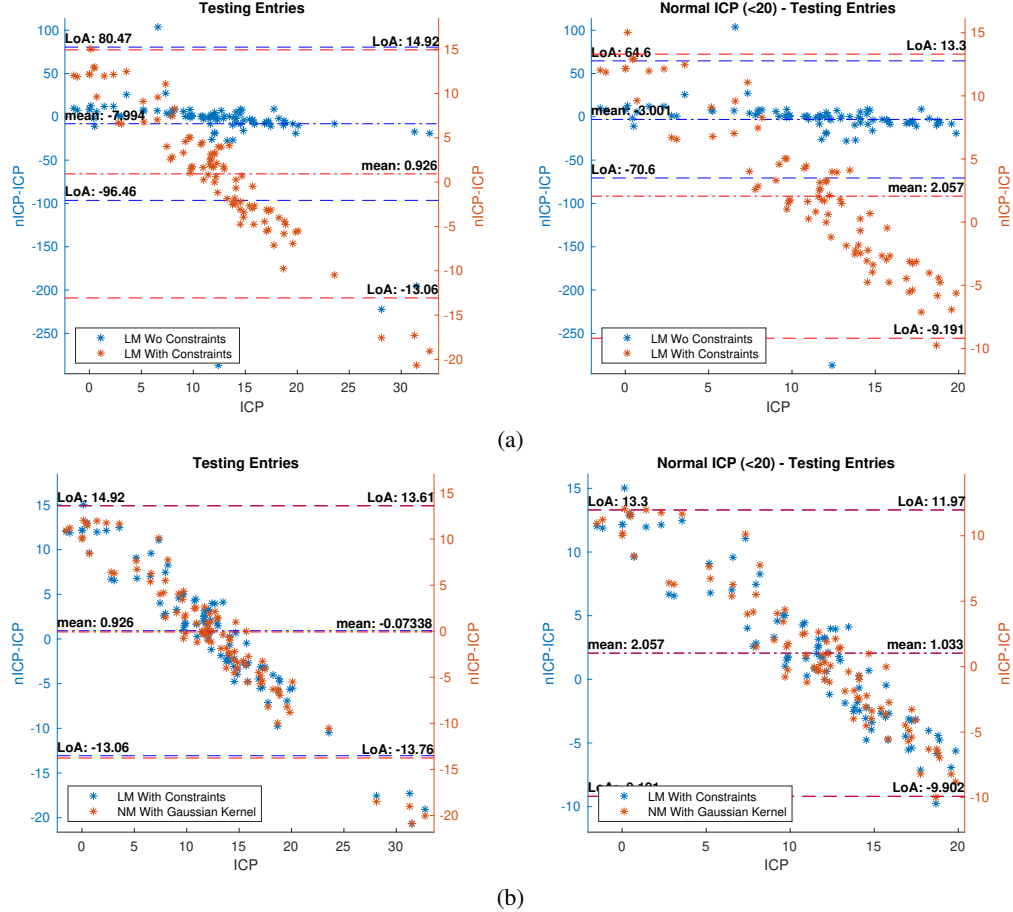


Figure 5: Bland–Altman plots for testing entries with comparisons from different algorithms. (a): Bland-Altman plot for nICP results comparisons between the linear mapping without constraints and linear mapping with constraints. (b): Bland-Altman plot for nICP results comparisons between the linear mapping with constraints and nonlinear mapping. Values on the left y-axis represent the results from data points in blue. Values on the right y-axis in the images represent the results from data point in orange. ‘LM Wo Constraints’ stands for the linear mapping without constraints. ‘LM With Constraints’ stands for the linear mapping with constraints. ‘NM With Gaussian Kernel’ stands for nonlinear mapping with Gaussian kernel.

4.2 Ranking Constraints Analysis

Fig. 9 illustrates the Kendall correlation between the errors from the mapping functions and those from the identified systems. For ground truth mean ICP values within the normal range (e.g., 11.78 mmHg or 13.81 mmHg), the nonlinear mappings using polynomial and Gaussian kernels achieve comparable Kendall correlation coefficients with smaller errors, whereas the linear mapping without constraints produces the lowest correlation and the highest estimation error. This finding indicates that incorporating ranking constraints is highly effective for estimating normal ICP, yielding improvements of at least 90%.

5 Discussion

Our solution for a practical and potential nICP technology creatively integrates machine learning and dynamic system identification to provide individualized calibration. Individualization is realized by a novel idea based on learning “mapping functions” that estimate nICP prediction errors associated with identified linear dynamic models (LDMs) within a pre-established database. Ranking available LDMs based on the estimated nICP errors determines the optimal model to simulate ICP for individual cases. When the case database lacks cases representative of a test instance, the optimal LDM may produce inaccurate nICP estimation. Learning the mapping-functions was challenging until a recent breakthrough. This breakthrough incorporates novel algorithmic components that go beyond conventional

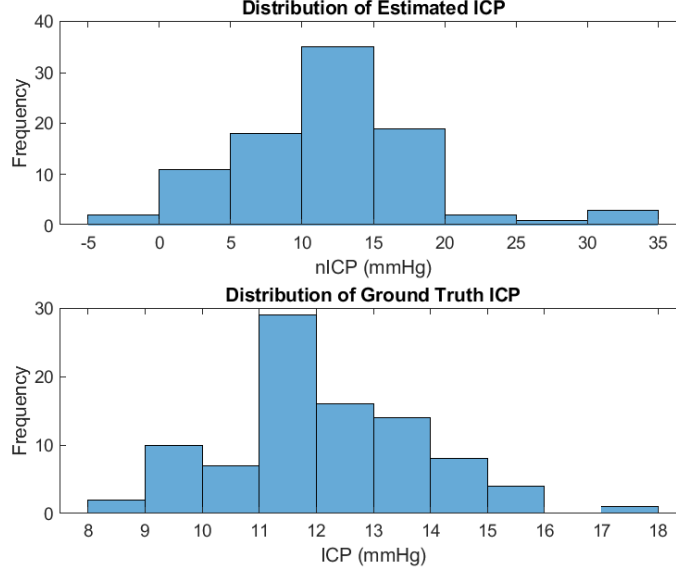


Figure 6: Distribution of estimation ICP and ground truth ICP from nonlinear mapping with Gaussian kernel.

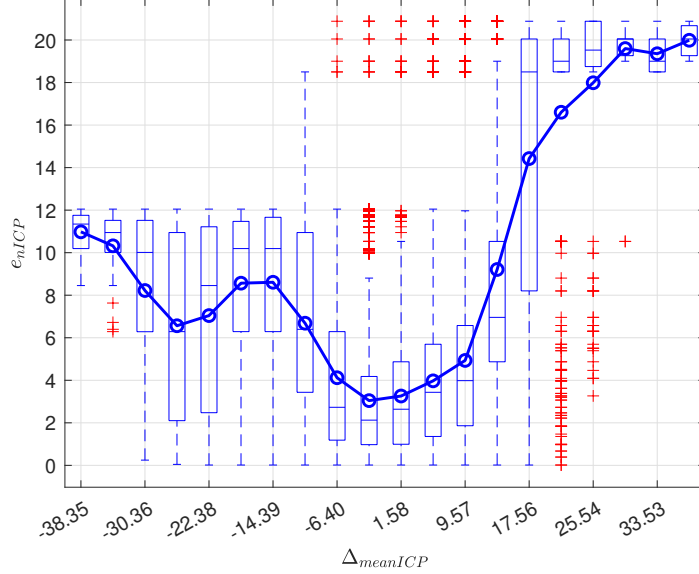


Figure 7: Box plot of the nICP estimation error in terms of the mean ICP difference between the testing entries and the training entries. ‘o’ stands for the mean value of each bin.

neural networks based machine learning methods. In particular, this mapping-function learning problem cannot be solved by simply using off-the-shelf machine-learning techniques. Instead, problem-specific information needs to be incorporated to find a solution. Our past efforts used algorithms such as linear regression Prunet et al. [2012], support vector machines Razumovsky and Armonda [2011], and spectral regressions Hu et al. [2010] to independently estimate mapping-function for each LDM. Such efforts were met with moderate success because ranking constraints were not considered in the learning process. Incorporating ranking constraints, however, presents a practical challenge. Therefore, we designed an approximate but computationally efficient solution. To our knowledge, this paper will be the first to adopt a bespoke machine learning algorithm specifically designed to address the key challenges inherent in noninvasive ICP estimation.

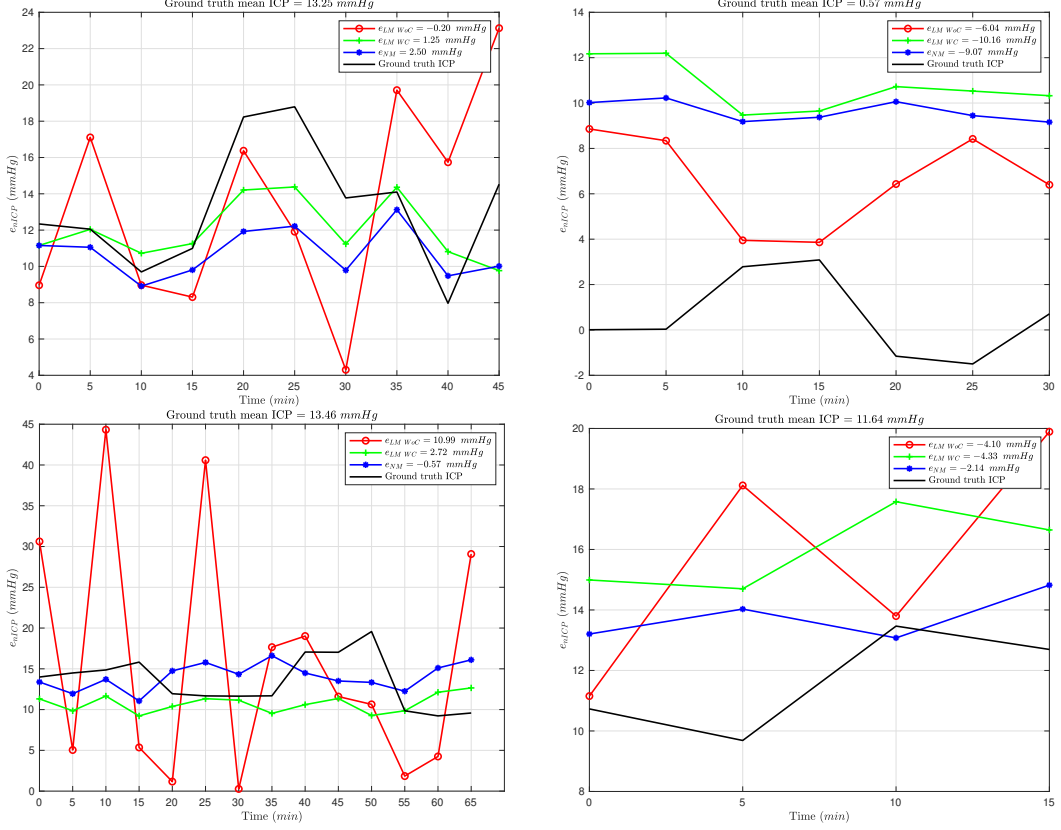


Figure 8: Error plots for various testing entries with N1-Median from different algorithms. From left to right: (1): testing entry with ground truth mean ICP = 13.25 mmHg, (2): testing entry with ground truth mean ICP = 0.57 mmHg. (3): testing entry with ground truth mean ICP = 13.46 mmHg, (4): testing entry with ground truth mean ICP = 11.64 mmHg. $e_{LM\ WoC}$ stands for the estimation error from linear mapping without constraints. $e_{LM\ WC}$ stands for the estimation error from linear mapping with constraints. e_{NM} stands for the estimation error from nonlinear mapping.

We also propose to use morphological metrics derived from CBv pulse as input features to mapping-functions. While the influence of ICP on CBv pulse morphology is well known De Cock and De Moor [2002], most existing approaches for relating CBv to ICP are focused on the single pulsatility index (PI). PI only provides amplitude information of CBv pulses, and its performance for nICP assessment is inconsistent Cuturi and Doucet [2011], Gönen and Alpaydin [2011]. In contrast, this study adopts the MOCAIP algorithm Aggarwal et al. [2008] for CBv signal analysis. In addition to CBv pulse morphological metrics, impulse response features extracted from the R-R interval, ABP, and CBv, as well as the latency and cerebral compliance features, are adopted as input features to the mapping functions.

A database of multimodality monitoring signals from 156 patients across six institutions is built as the training and testing database. The trained mapping function shows promising nICP estimation accuracy for normal ICP ranges, achieving errors within 6 mmHg for approximately 69% of measurements. The results also indicate that our approach is grounded in the physiological dynamic relationships among CBv, ABP, and R-R interval, which are common in brain conditions, leading to reasonable intracranial pressure estimation under specific conditions.

However, our analysis reveals a critical limitation: the framework systematically underestimates elevated ICP (>20 mmHg) with a mean error of -15.74 mmHg for nonlinear mapping and -15.09 mmHg for linear mapping with constraints. For entries with hypertension, the model tends to underestimate the ICP, as most of the ICP values in the training data are distributed within the range of 12 – 14 mmHg. It turns out that a few entries are distributed within the high ICP range, which leads to inaccurate nICP estimation. Additionally, data quality assessment remains an important challenge in the feature extraction of the signals, especially for the TCD signal. Whether TCD signals are effective for noninvasive monitoring of intracranial pressure is still under debate Cardim et al. [2016]. The TCD signal is highly sensitive to variations caused by probe placement and must be handled by well-trained technicians, which can lead to noise and artifacts. Recent studies show that transcranial signal can also be obtained by using a conformal ultrasound patch Zhou et al. [2024], which could support the development of noninvasive intracranial

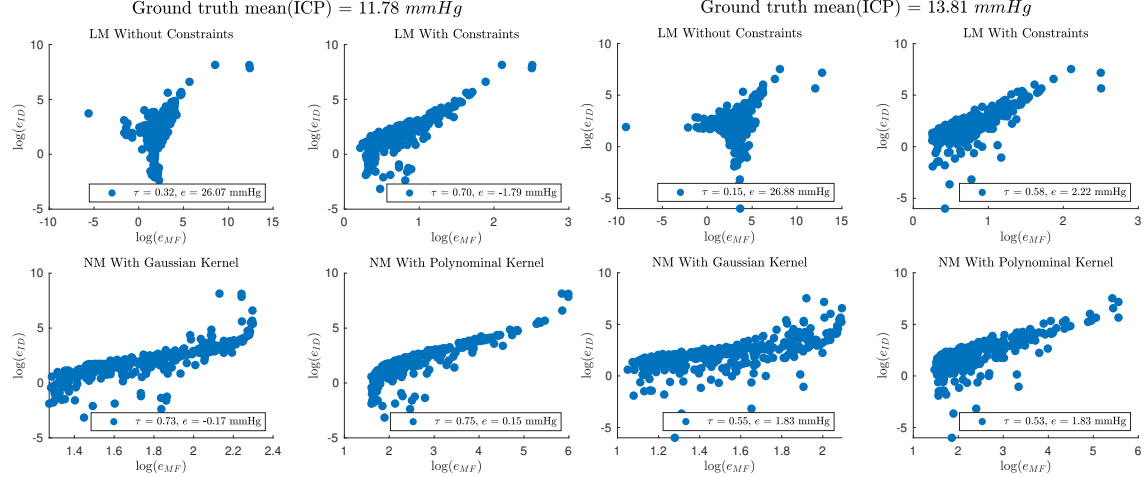


Figure 9: Error plots for various testing entries with N1-Median, illustrating the performance achieved by incorporating the constraints. ‘LM’ stands for ‘Linear Mapping’, ‘NM’ stands for ‘Nonlinear Mapping’. e_{ID} stands for the errors from the identified models. e_{MF} stands for the errors from the mapping functions.

pressure estimation through improved hardware and potentially reduce operator dependence. The developed approach is not limited to TCD signals. It can also be applied to other noninvasive physiological signals that reflect ICP through brain hemodynamics, such as near-infrared spectroscopy (NIRS). In this study, we illustrate the feasibility of the method using TCD signals as a representative example, demonstrating how our proposed approach can extract ICP-related information from hemodynamic measurements. Besides the TCD signals, the type of ICP monitoring can also affect the final results, since mis-leveling can introduce hydrostatic offsets. Furthermore, optimization algorithms may need to be developed to select the optimal hyperparameters for improving the performance of nICP estimation.

For clinical translation, a kernel-warping procedure could be developed to incorporate the input feature of a *de novo* instance to obtain a data-dependent kernel. Moreover, further investigation is needed to understand how patient-specific features influence the nICP estimation error. A calibration function can be developed to establish the relationship between the error from the mapping function and the true nICP estimation error to properly handle *de novo* instances in clinical practice. Further physiologically based constraints can also be considered during the system identification and mapping function training procedures. As demonstrated by physics-informed neural networks in physiological signal modeling and processing Zhao et al. [2025], incorporating physics constraints into the training process of machine learning models can significantly improve the performance of prediction.

6 Conclusion

This study introduces a novel framework for nICP estimation based on machine learning algorithms incorporating ranking constraints. Accurate and continuous estimation of intracranial pressure is crucial for managing patients with neurological disorders, however, invasive monitoring techniques remain the clinical standard, limiting their routine application due to associated risks. The proposed framework aims to bridge this gap by leveraging multimodal physiological signals and advanced learning strategies to achieve noninvasive estimation. For validation, we used an available multimodality monitoring database including ABP, CBFV, and invasive ICP signals from 156 patients across six institutions; while not exhaustive, it offers a useful starting point for assessment. The proposed method demonstrated promising performance, achieving certain estimation accuracy across diverse clinical conditions and institutions. Preliminary results confirm the feasibility and generalizability of the ranking-constrained learning approach for noninvasive ICP monitoring. Nevertheless, further research is required to refine model interpretability and clinical applicability, especially for patients with intracranial hypertension. Future work will focus on in-depth analysis of elevated ICP, extraction of additional morphological and physiological features, systematic hyperparameter optimization, and the development of patient-specific kernels to capture individual cerebrovascular dynamics.

References

Cameron Allan Gunn, Xiao Hu, and Lieven Vandenberghe. Artifact rejection and missing data imputation in cerebral blood flow velocity signals via trace norm minimization. *Physiological Measurement*, 41(11):114003, 2020.

Nancy Carney, Annette M. Totten, Cindy O'Reilly, Jamie S. Ullman, Gregory W. J. Hawryluk, Michael J. Bell, Susan L. Bratton, Randall Chesnut, Odette A. Harris, and Niranjan Kissoon. Guidelines for the management of severe traumatic brain injury. *Neurosurgery*, 80(1):6–15, 2017.

Gregory W. J. Hawryluk, Andres M. Rubiano, Annette M. Totten, Cindy O'Reilly, Jamie S. Ullman, Susan L. Bratton, Randall Chesnut, Odette A. Harris, Niranjan Kissoon, and Lori Shutter. Guidelines for the management of severe traumatic brain injury: 2020 update of the decompressive craniectomy recommendations. *Neurosurgery*, 87(3):427–434, 2020.

Susan L. Bratton, Randall M. Chestnut, Jamshid Ghajar, Flora F. McConnell Hammond, Odette A. Harris, Roger Hartl, Geoffrey T. Manley, Andrew Nemecek, David W. Newell, and Guy Rosenthal. Vi. indications for intracranial pressure monitoring. *Journal of Neurotrauma*, 24(Suppl 1):S37–S44, 2007.

Canac Nicolas, Jalaleddini Kian, G. Thorpe Samuel, M. Thibeault Corey, and B. Hamilton Robert. Review: Pathophysiology of intracranial hypertension and noninvasive intracranial pressure monitoring. *Fluids and Barriers of the CNS*, 17(40), 2020.

Pablo del Saz-Saucedo, Olga Redondo-González, Ángel Mateu-Mateu, Rafael Huertas-Arroyo, Rafael García-Ruiz, and Enrique Botia-Paniagua. Sonographic assessment of the optic nerve sheath diameter in the diagnosis of idiopathic intracranial hypertension. *Journal of the neurological sciences*, 361:122–127, 2016. ISSN 0022-510X.

Erdal Komut, Nalan Kozacı, Bedriye Müge Sönmez, Fevzi Yılmaz, Seval Komut, Zeliha Nilgün Yıldırım, İnan Beydilli, and Cihat Yel. Bedside sonographic measurement of optic nerve sheath diameter as a predictor of intracranial pressure in ed. *The American journal of emergency medicine*, 34(6):963–967, 2016. ISSN 0735-6757.

M. Motschmann, C. Müller, J. Kuchenbecker, S. Walter, K. Schmitz, M. Schütze, W. Behrens-Baumann, and R. Firsching. Ophthalmodynamometry: A reliable method for measuring intracranial pressure. *Strabismus*, 9(1):13–16, 2001.

Tomasz Czarnik, Ryszard Gawda, Dariusz Łatka, Waldemar Kołodziej, Katarzyna Sznajd-Weron, and Rafał Weron. Noninvasive measurement of intracranial pressure: Is it possible? *Journal of Trauma and Acute Care Surgery*, 62(1):207–211, 2007.

Miaomiao Wei, Solventa Krakauskaitė, Ryan Mercer, Jiaguo Lin, Laimonas Bartusis, and Fabien Scalzo. Noninvasive intracranial hypertension detection using machine-learning of cerebral blood flow velocity waveforms. SSRN 5148598, 2025.

Frank A. Rasulo, Stefano Calza, Chiara Robba, Fabio Silvio Taccone, Daniele G. Biasucci, Rafael Badenes, Simone Piva, Davide Savo, Giuseppe Citerio, and Jamil R. Dibu. Transcranial doppler as a screening test to exclude intracranial hypertension in brain-injured patients: The IMPRESSIT-2 prospective multicenter international study. *Critical Care*, 26(1):110, 2022.

Ronney B Panerai, Patrice Brassard, Joel S Burma, Pedro Castro, Jurgen AHR Claassen, Johannes J van Lieshout, Jia Liu, Samuel JE Lucas, Jatinder S Minhas, and Georgios D Mitsis. Transfer function analysis of dynamic cerebral autoregulation: a carnet white paper 2022 update. *Journal of Cerebral Blood Flow & Metabolism*, 43(1):3–25, 2023. ISSN 0271-678X.

Toshiaki Ueno, Richard E. Ballard, Brandon R. Macias, William T. Yost, and Alan R. Hargens. Cranial diameter pulsations measured by non-invasive ultrasound decrease with tilt. *Aviation, Space, and Environmental Medicine*, 74(8):882–885, 2003.

Fernando Pose, Carlos Videla, Giovanni Campanini, Francisco O. Redelico, and Nicolas Ciarrocchi. A pilot study for continuous non-invasive intracranial pressure screening. *Computers in Biology and Medicine*, 186:109611, 2025.

Oliver Ganslandt, Stylianos Mourtzoukos, Andreas Stadlbauer, Björn Sommer, and Rudolf Rammensee. Evaluation of a novel noninvasive ICP monitoring device in patients undergoing invasive ICP monitoring: Preliminary results. *Journal of Neurosurgery*, 128(6):1653–1660, 2017.

Martin W. Herklots, Walid Moudrous, Annemarie Oldenbeuving, Gerwin Roks, Stylianos Mourtzoukos, Guus G. Schoonman, and Oliver Ganslandt. Prospective evaluation of noninvasive headsense intracranial pressure monitor in traumatic brain injury patients undergoing invasive intracranial pressure monitoring. *World Neurosurgery*, 106:557–562, 2017.

Mauro Oddo, Fabio S Taccone, Matteo Petrosino, Rafael Badenes, Aaron Blandino-Ortiz, Pierre Bouzat, Anselmo Caricato, Randall M Chesnut, Anders C Feyling, and Nawfel Ben-Hamouda. The neurological pupil index for outcome prognostication in people with acute brain injury (orange): a prospective, observational, multicentre cohort study, 2023.

Waleed Aletreby, Abdulrahman Alharthy, Peter G Brindley, Demetrios J Kutsogiannis, Fahad Faqih, Waseem Alzayer, Abdullah Balhahmar, Ibrahim Soliman, Hend Hamido, and Saleh A Alqahtani. Optic nerve sheath diameter ultrasound for raised intracranial pressure: a literature review and meta-analysis of its diagnostic accuracy. *Journal of ultrasound in medicine* 41, 585-595 (2022). *Journal of Ultrasound in Medicine*, 41(3):585–595. ISSN 0278-4297.

Karol Martínez-Palacios, Sebastián Vásquez-García, Olubunmi A Fariyike, Chiara Robba, and Andrés M Rubiano. Using optic nerve sheath diameter for intracranial pressure (ICP) monitoring in traumatic brain injury: a scoping review, 2024.

Gustavo Frigieri, Sérgio Brasil, Danilo Cardim, Marek Czosnyka, Matheus Ferreira, Wellington S. Paiva, and Xiao Hu. Machine learning approach for noninvasive intracranial pressure estimation using pulsatile cranial expansion waveforms. *npj Digital Medicine*, 8(1):57, 2025a.

Gustavo Frigieri, Thauan Leandro Gonçalves, Gabriela Nagai Ocamoto, Rodrigo de Ap Andrade, Bruno Cezar de Padua, and Danilo Cardim. Clinical performance of the Brain4care system for noninvasive detection of intracranial hypertension. *Neurocritical Care*, pages 1–8, 2025b.

Sanem Pinar Uysal, Hayley G Williams, Mina Huerta, Nicolas R Thompson, and Catherine E Hassett. Noninvasive method using mechanical extensometer for the estimation of intracranial compliance by repeated measures agreement analysis. *Neurocritical Care*, 42(2):465–473, 2025.

Sérgio Brasil, Davi Jorge Fontoura Solla, Ricardo de Carvalho Nogueira, Manoel Jacobsen Teixeira, Luiz Marcelo Sá Malbouisson, and Wellington da Silva Paiva. A novel noninvasive technique for intracranial pressure waveform monitoring in critical care. *Neurocritical Care*, 11(12):1302, 2021.

Fabiano Moulin de Moraes, Eva Rocha, Felipe Chaves Duarte Barros, Flávio Geraldo Rezende Freitas, Maramelia Miranda, Raul Alberto Valiente, João Brainer Clares de Andrade, Feres Eduardo Aparecido Chaddad Neto, and Gisele Sampaio Silva. Waveform morphology as a surrogate for ICP monitoring: a comparison between an invasive and a noninvasive method. *Neurocritical Care*, 37(1):219–227, 2022.

Faisal M Kashif, George C Verghese, Vera Novak, Marek Czosnyka, and Thomas Heldt. Model-based noninvasive estimation of intracranial pressure from cerebral blood flow velocity and arterial pressure. *Science translational medicine*, 4(129):129ra44–129ra44, 2012. ISSN 1946-6234.

Syed M. Imaduddin, Andrea Fanelli, Frederick W. Vonberg, Robert C. Tasker, and Thomas Heldt. Pseudo-bayesian model-based noninvasive intracranial pressure estimation and tracking. *IEEE Transactions on Biomedical Engineering*, 67(6):1604–1615, 2019.

Andrea Fanelli, Frederick W Vonberg, Kerri L LaRovere, Brian K Walsh, Edward R Smith, Shenandoah Robinson, Robert C Tasker, and Thomas Heldt. Fully automated, real-time, calibration-free, continuous noninvasive estimation of intracranial pressure in children. *Journal of Neurosurgery: Pediatrics*, 24(5):509–519, 2019. ISSN 1933-0715.

Rohan Jaishankar, Andrea Fanelli, Aristotelis Filippidis, Thai Vu, James Holsapple, and Thomas Heldt. A spectral approach to model-based noninvasive intracranial pressure estimation. *IEEE journal of biomedical and health informatics*, 24(8):2398–2406, 2019. ISSN 2168-2194.

Karen Brastad Evensen, Michael O'Rourke, Fabrice Prieur, Sverre Holm, and Per Kristian Eide. Non-invasive estimation of the intracranial pressure waveform from the central arterial blood pressure waveform in idiopathic normal pressure hydrocephalus patients. *Scientific reports*, 8(1):4714, 2018. ISSN 2045-2322.

Murad Megjhani, Kalijah Terilli, Bennett Weinerman, Daniel Nametz, Soon Bin Kwon, Angela Velazquez, Shivani Ghoshal, David J. Roh, Sachin Agarwal, and E. Sander Connolly Jr. A deep learning framework for deriving noninvasive intracranial pressure waveforms from transcranial doppler. *Annals of Neurology*, 94(1):196–202, 2023.

George R. E. Bradley and Panayiotis A. Kyriacou. Evaluating the effectiveness of non-invasive intracranial pressure monitoring via near-infrared photoplethysmography using classical machine learning methods. *Biomedical Signal Processing and Control*, 96:106517, 2024.

George R. E. Bradley, María Roldán, and Panayiotis A. Kyriacou. Machine learning approaches to intracranial pressure prediction in patients with traumatic brain injury: A systematic review. *Applied Sciences*, 13(14):8015, 2023.

Tohru Katayama. *Subspace Methods for System Identification*, volume 1. Springer, Boston, 2005.

Isabel Martinez-Tejada, Marek Czosnyka, Zofia Czosnyka, Marianne Juhler, and Peter Smielewski. Causal relationship between slow waves of arterial, intracranial pressures and blood velocity in brain. *Computers in Biology and Medicine*, 139:104970, 2021. ISSN 0010-4825.

Xiao Hu, Peng Xu, Shaozhi Wu, Shadnaz Asgari, and Marvin Bergsneider. A data mining framework for time series estimation. *Journal of biomedical informatics*, 43(2):190–199, 2010. ISSN 1532-0464.

Xiao Hu, Peng Xu, Fabien Scalzo, Paul Vespa, and Marvin Bergsneider. Morphological clustering and analysis of continuous intracranial pressure. *IEEE Transactions on Biomedical Engineering*, 56(3):696–705, 2008.

Sunghan Kim, Marvin Bergsneider, and Xiao Hu. A systematic study of linear dynamic modeling of intracranial pressure dynamics. *Physiological Measurement*, 32(3):319, 2011a.

Sunghan Kim, Xiao Hu, David McArthur, Robert Hamilton, Marvin Bergsneider, Thomas Glenn, Neil Martin, and Paul Vespa. Inter-subject correlation exists between morphological metrics of cerebral blood flow velocity and intracranial pressure pulses. *Neurocritical Care*, 14:229–237, 2011b.

Xiaobin Xie, Xiaojun Zhang, Jidi Fu, Huaizhou Wang, Jost B. Jonas, Xiaoxia Peng, Guohong Tian, Junfang Xian, Robert Ritch, and Lei Li. Noninvasive intracranial pressure estimation by orbital subarachnoid space measurement: The Beijing intracranial and intraocular pressure (iCOP) study. *Critical Care*, 17:1–12, 2013.

Sunghan Kim, Robert Hamilton, Stacy Pineles, Marvin Bergsneider, and Xiao Hu. Noninvasive intracranial hypertension detection utilizing semisupervised learning. *IEEE Transactions on Biomedical Engineering*, 60(4):1126–1133, 2012. ISSN 0018-9294.

Walter Karlen, J. Mark Ansermino, and Guy Dumont. Adaptive pulse segmentation and artifact detection in photoplethysmography for mobile applications. In *2012 Annual International Conference of the IEEE Engineering in Medicine and Biology Society*, pages 3131–3134. IEEE, 2012. ISBN 978-1-4244-4119-8.

Davide Giavarina. Understanding Bland Altman analysis. *Biochimia Medica*, 25(2):141–151, 2015.

Karen Brastad Evensen and Per Kristian Eide. Measuring intracranial pressure by invasive, less invasive or non-invasive means: limitations and avenues for improvement. *Fluids and Barriers of the CNS*, 17(1), 2020. ISSN 2045-8118.

Bertrand Prunet, Yves Asencio, Guillaume Lacroix, Ambroise Montcriol, Arnaud Dagain, Jean Cotte, Pierre Esnault, Henry Boret, Eric Meaudre, and Eric Kaiser. Noninvasive detection of elevated intracranial pressure using a portable ultrasound system. *The American Journal of Emergency Medicine*, 30(6):936–941, 2012.

Alexander Razumovsky and Rocco A. Armonda. We still do not have a reliable and validated noninvasive technique that can provide an accurate quantitative measurement of intracranial pressure (ICP) that could replace invasive quantitative measurements of ICP. *Neurosurgery*, 68(1):E289–E292, 2011.

Katrien De Cock and Bart De Moor. Subspace angles between ARMA models. *Systems & Control Letters*, 46(4): 265–270, 2002. ISSN 0167-6911.

Marco Cuturi and Arnaud Doucet. Autoregressive kernels for time series. *arXiv*, 2011.

Mehmet Gönen and Ethem Alpaydin. Multiple kernel learning algorithms. *The Journal of Machine Learning Research*, 12:2211–2268, 2011. ISSN 1532-4435.

Shushma Aggarwal, David M. Brooks, Yoogoo Kang, Peter K. Linden, and John F. Patzer. Noninvasive monitoring of cerebral perfusion pressure in patients with acute liver failure using transcranial doppler ultrasonography. *Liver Transplantation*, 14(7):1048–1057, 2008.

Danilo Cardim, C. Robba, Michał Bohdanowicz, J. Donnelly, B. Cabella, X. Liu, M. Cabeleira, Piotr Smielewski, B. Schmidt, and Marek Czosnyka. Non-invasive monitoring of intracranial pressure using transcranial doppler ultrasonography: Is it possible? *Neurocritical Care*, 25:473–491, 2016.

Sai Zhou, Xiaoxiang Gao, Geonho Park, Xinyi Yang, Baiyan Qi, Muyang Lin, Hao Huang, Yizhou Bian, Hongjie Hu, and Xiangjun Chen. Transcranial volumetric imaging using a conformal ultrasound patch. *Nature*, 629(8013): 810–818, 2024.

Anni Zhao, Davood Fattah, and Xiao Hu. Physics-informed neural networks for physiological signals processing and modeling: a narrative review. *Physiological Measurement*, 2025. ISSN 0967-3334.